Review

Sensitivity of Field-Effect Transistor-Based Terahertz Detectors

Elham Javadi [1,*], Dmytro B. But [1,2], Kęstutis Ikamas [3,4], Justinas Zdanevičius [3], Wojciech Knap [1,2,5] and Alvydas Lisauskas [1,3,*]

[1] CENTERA Laboratories, Institute of High Pressure Physics PAS, 01-142 Warsaw, Poland; dbut@mail.unipress.waw.pl (D.B.B.); knap.wojciech@gmail.com (W.K.)
[2] CEZAMAT, Warsaw Technical University, 02-822 Warsaw, Poland
[3] Institute of Applied Electrodynamics and Telecommunications, Vilnius University, LT-10257 Vilnius, Lithuania; kestutis.ikamas@ff.vu.lt (K.I.); justinas.zet@gmail.com (J.Z.)
[4] Research Group on Logistics and Defense Technology Management, General Jonas Žemaitis Military Academy of Lithuania, LT-10322 Vilnius, Lithuania
[5] Laboratoire Charles Coulomb, University of Montpellier, and CNRS, 34095 Montpellier, France
* Correspondence: ejavadi@mail.unipress.waw.pl (E.J.); alvydas.lisauskas@ff.vu.lt (A.L.)

Abstract: This paper presents an overview of the different methods used for sensitivity (i.e., responsivity and noise equivalent power) determination of state-of-the-art field-effect transistor-based THz detectors/sensors. We point out that the reported result may depend very much on the method used to determine the effective area of the sensor, often leading to discrepancies of up to orders of magnitude. The challenges that arise when selecting a proper method for characterisation are demonstrated using the example of a 2×7 detector array. This array utilises field-effect transistors and monolithically integrated patch antennas at 620 GHz. The directivities of the individual antennas were simulated and determined from the measured angle dependence of the rectified voltage, as a function of tilting in the E- and H-planes. Furthermore, this study shows that the experimentally determined directivity and simulations imply that the part of radiation might still propagate in the substrate, resulting in modification of the sensor effective area. Our work summarises the methods for determining sensitivity which are paving the way towards the unified scientific metrology of FET-based THz sensors, which is important for both researchers competing for records, potential users, and system designers.

Keywords: THz detectors; planar antennas; focal plane arrays; effective antenna area; CMOS detector

Citation: Javadi, E.; But, D.B.; Ikamas, K.; Zdanevičius, J.; Knap, W.; Lisauskas, A. Sensitivity of Field-Effect Transistor-Based Terahertz Detectors. *Sensors* **2021**, *21*, 2909. https://doi.org/10.3390/s21092909

Academic Editor: Ahmed Toaha Mobashsher

Received: 14 March 2021
Accepted: 16 April 2021
Published: 21 April 2021

Publisher's Note: MDPI stays neutral with regard to jurisdictional claims in published maps and institutional affiliations.

Copyright: © 2021 by the authors. Licensee MDPI, Basel, Switzerland. This article is an open access article distributed under the terms and conditions of the Creative Commons Attribution (CC BY) license (https://creativecommons.org/licenses/by/4.0/).

1. Introduction

For a considerably long time, devices that utilise thermal detection principles have been routinely employed as practical detectors in the terahertz (THz) frequency range. The prominent representatives of this class are Golay cells [1], pyroelectric detectors [2], and bolometers [3]. As the radiation can be delivered to the sensing element employing the absorption mechanism, the performance of thermal detectors can be well-calibrated and traced [2]. However, a number of particular characteristics related to thermal detection mechanisms, such as low modulation speed, comparatively large area, and the need for external filters if detector frequency selectivity is required, pose severe limitations for the applicability of such devices. Another class of uncooled THz detectors includes the zero-bias Schottky barrier detector [4–6] and the recently emerged family of detectors based on field-effect transistors (FETs). The fast response time, in conjunction with the high sensitivity values of the latter class of devices, makes rectifiers very attractive for practical applications. Furthermore, FET-based detectors profit from integrated circuit technological development and can be produced in large arrays [7–11].

The main principle of efficient THz FET detector operations at frequencies highly exceeding the transistor cut-off limit relies on the excitation of damped plasma oscillations in a two-dimensional gas in the transistor channel [12–15]. This mechanism was later

extended to a device model based on hydrodynamic transport description, in order to account for rectification efficiency and device impedance [16–19].

It is important to note that, with the introduction of novel detection mechanisms, new challenges for researchers, in terms of determining traceable ways to present their performance values, have appeared. The main challenge arises from the fact that the rectifying part of the FET—an ordinary object of study—is much smaller (often with sub µm dimensions) than the THz wavelength (hundreds of µm). Therefore, the THz radiation has to be coupled to it using a grating or either intentional or unintentional antennae, which defines the effective detector area in the process of sensitivity determination. Compared with two-terminal devices, such as Schottky diodes, which benefit from the developed solutions for integration into metal waveguides, there exist no ready solutions for three-terminal transistors. Therefore, initial proof-of-principle experiments have been performed using discrete FETs [12,13,20]. A report of the efficient detection of 700 GHz radiation using wire-bonded 120 nm CMOS devices [21] has raised exceptional attention. As discrete devices possess no dedicated antennas, the assumption is made that the fraction of the power delivered to the device is proportional to the diffraction-limited spot. However, a comprehensive study performed much later using discrete GaAs devices brought attention to the fact that both the structure of contacts and bonding wires play unintentional roles as antennas. The performance estimates based on the antenna-related effective area and that of the diffraction-limited spot may differ by more than 18 times [22].

The first array, which combined complementary metal–oxide–semiconductor (CMOS) FETs with on-chip integrated antennas, was developed using a 250 nm technology node [14]. The array consisted of 3×5 pixels with resonant patch antennas and on-chip integrated amplifiers and reported a responsivity of 70 kV/W and a noise equivalent power (NEP) of 300 pW/$\sqrt{\text{Hz}}$ at 30 kHz chopping frequency. Although these devices contained antennas for which the effective areas could have been simulated using a standard approach, it was assumed that, due to the proximity of neighbouring detectors and concomitant power-sharing, the effective area is set by the pitch between devices. Further optimisations have been performed for the antenna, as well as the device; for example, the employment of 65 nm CMOS SOI technology resulted in an improvement in NEP values to $\sim$50 pW/$\sqrt{\text{Hz}}$ at 650 GHz [23] or 20 pW/$\sqrt{\text{Hz}}$ at 590 GHz [24] for a 90 nm CMOS process with the assumption of effective areas supported by electromagnetic simulations.

Evaluation of the performance for substrate-lens coupled devices poses another challenge, as the full-wave simulation of structures at THz frequencies requires invoking computer resources that are hardly accessible. One of the first reports on detectors that utilise broadband antennas with preferred coupling direction from the substrate side was presented in [7] for a 32×32 pixel array fabricated using 65 nm CMOS technology. Although the reported minimum NEP of $\sim$100 pW/$\sqrt{\text{Hz}}$ at 856 GHz was slightly larger than that for resonant devices, a bandwidth of 200 GHz was achieved.

Much progress has been reported in terms of improving the optical performance of devices implemented using CMOS technologies. For example, employing biquad antennas allows for reaching $\sim$25 pW/$\sqrt{\text{Hz}}$ at 1 THz with more than 400 GHz bandwidth [25], or larger than 1 THz bandwidth with $\sim$50 pW/$\sqrt{\text{Hz}}$ for the bow-tie antenna-coupled detectors [26], which are competitive to commercial quasioptical Schottky diode detectors [27]. In parallel to the progress in silicon technology-based devices, sensitive detectors have been produced using field-effect transistors fabricated using III–V technologies, mono- and bilayer graphene, as well as by invoking other detection principles, such as ballistic transport [28] or thermoelectric currents [29–31]. It is also important to note that the presented FET NEP values gradually approach the level of Schottky diodes, with NEP values of a few pW/$\sqrt{\text{Hz}}$ at room temperature. For a more detailed discussion of various types of terahertz detectors, we recommend the following review works [32,33].

One can note that, depending on the purpose of the device, such as designing a single detector; serving as part of an array or as an imaging element; providing optimal point-to-point power delivery; or proof-of-the-principle for a novel structure or detection

phenomena, it is often required to apply different methods to specify the main figures-of-merit. This manuscript summarises six main methods reported in the recent literature and addresses the differences between them. Furthermore, it summarises the performance values and characterisation methods used for state-of-the-art devices in three material system-related groups: Silicon, III–V semiconductors, and novel low-dimensional structures. Finally, we present a comprehensive simulation-supported experimental study of devices implemented in a 2×7 array using 65 nm CMOS and illustrate the spread of performance values under different methods.

2. Commonly Used Methods for the Estimation of THz Detector Area

Based on our review, performed on over 50 state-of-the-art field-effect transistor-based detectors, we outline six methods commonly used to estimate the THz detector area in the following. The summary of methods, with reference to the relative reports, is presented in Table 1.

Table 1. Summary of methods used for estimation of the effective area of THz detectors.

Method for calculation of A_{eff}	Comment	Ref.
I. From the antenna gain	$A_{\text{eff}} = \frac{G\lambda_0^2}{4\pi}$ This is a widely accepted method in the field of microwave antennas, which has been described in textbooks and simulation tools. It accounts for the power loss due to antenna efficiency and allows for estimating the power which is applied to the detector circuit.	[34–37], [[38] pp. 1–10]
II. From the maximal directivity	$A_{\text{eff}} = \frac{D\lambda_0^2}{4\pi}$ This definition describes the maximum antenna effective aperture. Therefore, it is best suited for the determination and comparison of optical characteristics of detectors.	[17,19,24,39–47], [[48] p. 92]
III. Physical area	In multipixel imaging arrays with overlapping effective areas, the detector pixel size can be approximated by the pitch between devices. However, it must be assured that the devices do not form a dielectric antenna structure. In some works, the physical area has been specified as the aperture of the substrate lens.	[9–11,23,39,49–57]
IV. Area of the diffraction-limited spot	$A_{\text{diff}} = \frac{\lambda_0^2}{4}$ This area is often used for devices without dedicated antennas. It has been claimed to be a conservative estimate; however, in most cases, it leads to the substantial overestimation of detector performance.	[31,58–65]
V. Normalised for the omnidirectional antenna case	$A_{\text{omni}} = \frac{\lambda_0^2}{4\pi}$ This area is used for devices with known (simulated or measured) directivity, by normalising it to unity for the omnidirectional antenna case (in other words, the antenna gain is de-embedded) and, for devices without dedicated antennas, it is interpreted as a circular-shaped diffraction-limited spot.	[28,66–70]
VI. Without any normalisation	The optical performance without normalisation of the incident power is relevant for a wide range of applications, such as raster-scan imaging, spectroscopy, and other systems exploiting point-to-point configurations. The performance values obtained in this way can be compared with that of commercially available devices, such as bolometers, Golay cells, pyroelectric sensors, or quasioptically coupled Schottky diode detectors.	[26,29,71–80]

From the antenna gain. Probably the most accepted method in the field of microwave antennas is relating the effective area of the antenna, $A_{\text{eff,I}} = G\lambda_0^2/4\pi$, with its gain G and free-space wavelength λ_0 [38] [p. 1–10]. This method has been described in textbooks and simulation tools. The antenna gain and directivity D are directly related by the antenna efficiency η (i.e., $G = \eta D$). If the intensity, I_{THz}, of radiation at the plane of the detector is known—for example, when performing direct measurements or estimating it using the gain of the antenna used at the THz source side—one can estimate the power which is delivered into the detector circuit as $P_D = A_{\text{eff,I}} I_{\text{THz}}$. As a matter of fact, it is essential to estimate P_D, as well as the power matching coefficient and other related quantities, in order to perform

a quantitative comparison between the analytical CAD-based simulation, which usually starts from the intrinsic device or phenomenon description, and the experiment; however, in contrast to microwave frequency range-related instrumentation, at present, one can hardly detach the THz rectifying transistor from its antenna, nor exchange or independently characterise the THz properties of different constituents of the detector, except by performing simulations. Therefore, for comparing different implementations of THz detectors, it is more appropriate to use the power incident on the effective area.

From the maximal directivity. Knowing the maximal value of the directivity of the antenna allows for estimating the maximal effective area, which can be associated with the antenna $A_{\mathrm{eff,II}} = D\lambda_0^2/4\pi$. This does not determine the power delivered into the rectifying device's circuit but allows for estimation of the power which is incident on the antenna's effective area. Furthermore, the antenna's directivity can be both simulated and experimentally assessed, thus providing a reasonable quantity for comparing different devices or implementations.

Physical area. The directivity-defined effective areas of individual antennas can sometimes overlap, when the antenna-coupled detectors are arranged in a multipixel imaging array. In this case, the size of the detector pixel can be approximated by the pitch between devices. In Reference [23], arguments have been presented which show that this method, which uses the modeled directivity (as required for method II), predicts the same effective area as the pitch between the pixels. Later in this manuscript, we present experimental evidence that such equality between methods does not apply to devices located at the array's edges. Furthermore, it must be assured that the devices do not form a dielectric antenna structure. One example of such a case has been reported for a two-dimensional array of detectors that were designed for broadband detection above 600 GHz, which resulted in an unexpectedly enhanced local response at 300 GHz [81]. The physical area is sometimes specified as the lens's aperture; however, the term "physical" may be confused with the area of the metal [82] or the area of the structure having subwavelength dimensions, as for grating-coupled devices [55,83] or when considering the area of antenna slot [84].

Area of the diffraction limited spot. The area of the diffraction-limited spot, $A_{\mathrm{diff}} = \lambda_0^2/4$, has been often used for devices either without dedicated antennas or by contrast, in order to provide a more conservative estimate, compared to the physical area of elements with the subwavelength dimensions [85]. However, in the referenced paper, the authors defined the diffraction-limited spot area as $A_{\mathrm{diff}} = \lambda_0^2/\pi$. Moreover, these arguments do not address the involved mechanism of radiation coupling and do not allow for quantitative comparisons, reducing the result to the statement whether the devices are suitable for practical operation.

Normalised for the omnidirectional antenna case. There have been reports in the recent literature in which the authors presented the so-called gain or directivity de-embedded device characteristics for the omnidirectional antenna case (i.e., $A_{\mathrm{omni}} = \lambda_0^2/4\pi$). This area is a factor of π smaller than A_{diff} and sometimes is interpreted as a circular-shaped diffraction-limited spot; however, the detrimental difference between both methods is that the authors presented either the simulated or experimentally estimated antenna directivity D value, thus making the report traceable. However, although this quantity has started to gain popularity in the engineering community, it can hardly improve upon the credibility of later reports as, for now, the main improvement in detector sensitivity comes from the comparison to performance values reported without the de-embedding procedure. This becomes obvious when performing a scrutinous check of the comparison tables reported in [67,69,70].

Without any normalisation. There are a wide range of applications, such as raster-scan imaging, spectroscopy, and other systems that exploit point-to-point configuration, which require the detector's maximal sensitivity, regarding the total power, to be available in the directed (collinear) THz radiation beam. It is worth noting that, although a detector can be adequately characterised using the above-mentioned traceable methods, the optimum THz radiation coupling might require substituting the substrate lens with a different one. In such cases, as well as for direct comparison with the optical performance of calibrated

commercially available devices, such as bolometers, Golay cells, pyroelectric sensors, or quasioptically coupled Schottky diode detectors, one can present the performance of optimised devices by referring to the power of the beam (i.e., without imposing any assumptions on the detector area).

Furthermore, there have been reports on different methods which can be used in order to estimate the effective area of the detector; for example, by performing the deconvolution of recorded images (i.e., by numerical analysis of the measured spatial intensity distributions of the THz beam by employing fast Fourier transforms or the Richardson Lucy algorithm) [86,87].

Continuing the discussion about sensitivity estimation methods, it should become evident that all summarised methods that rely on evaluating the effective area can be treated as legitimate, if the authors provide information on the directivity of the detector or an equivalent traceable measurement of the effective area.

In the following, we present a summary of state-of-the-art detector performance values reported for devices implemented using silicon technologies (Table 2), using III–V material systems (Table 3) or involving novel low-dimensional structures (Table 4).

Table 2. Summary of reports on silicon-based THz detectors.

Technology	Freq.	Antenna	NEP	Responsivity	Single or Array	Method-Ology *	Ref.
	GHz		pW/$\sqrt{\text{Hz}}$	V/W			
MOSFET, 90 nm CMOS	250	Slot + Si lens	21	408	Single	VI	[80]
MOSFET, 90 nm CMOS	250–750	Various	40	185 k **	Single	II	[45]
HBT, 130 nm SiGe	292	Wire ring + Si lens	1.9	9 k	Single	V	[67]
MOSFET, 90 nm CMOS	300	Slot + Si lens	20.8	55 k **	Single	VI	[88]
MOSFET, 90 nm CMOS	300–1500	Bow-tie + Si lens	48–70	45	Single	VI	[26]
MOSFET, 65 nm CMOS	315	CSDRA	3.5	2 k	Single	II	[46]
HBT, 130 nm SiGe	430	Wire-ring +Si lens	2.7	5 k	Single	V	[68]
MOSFET, 90 nm CMOS	590	Patch	20	-	Single	II	[24]
MOSFET, 150 nm CMOS	595	Patch	42	350	Single	II	[17]
MOSFET, 130 nm CMOS	600	Bow-tie	25.9	216 k **	Array 31 × 31	III	[9]
MOSFET, 150 nm CMOS	600	Patch	43	300	Array 24 × 24	III	[10]
MOSFET, 22 nm FD-SOI CMOS	605	Double-folded dipole + Si lens	2.3	32 k	Single	V	[69]
MOSFET, 65 nm SOI CMOS	650	Folded dipole + Si lens	17	1930	Array 3 × 5	III	[51]
MOSFET, 130 nm SiGe BiCMOS	650	Ring + Si lens	80	450	Single	III	[50]
MOSFET, 250 nm CMOS	650	Patch	300	80 k **	Array 3 × 5	III	[53]
HBT, 250 nm SiGe	700	Ring + Si lens	50	1 A/W	Array 3 × 5	II	[39]
MOSFET, 65 nm Si CMOS	724	Ring + Si lens	14	2200	Single	III	[49]
P-N diode, 45 nm CMOS	781	Patch	56	558	Single	II	[43]
Diode-connected MOSFET, 130 nm CMOS	823	Patch	36.2	2560	Array 8 × 8	III	[52]
MOSFET, 22 nm FD-SOI CMOS	855	Ring + Si lens	12	0.180 [A/W]	Single	I	[37]
MOSFET, 180 nm CMOS	860	Patch	106	3300	Array 3 × 5	II	[40]
SBD, 130 nm CMOS	860	Patch	42	273	Single	II	[41]
MOSFET, 65 nm CMOS	1000	Bi-quad + Si lens	25	765	Single	VI	[25]
MOSFET, 90 nm CMOS	2520 3110 4250	Patch	63 85 110	336 308 230	Single	II	[8]
MOSFET, 65 nm CMOS	3000	Patch	73	526	Array 12 × 9	II	[47]
MOSFET, 65 nm CMOS	**620**	**Patch**	**19.2**	**1400**	**Array 2 × 7**	**II**	**This work**

* See Table 1. ** Amplified read-out was used for calculation of responsivity.

Table 3. Summary of reports on III–V THz detectors.

Technology	Freq.	Antenna	Min. NEP	Responsivity	Single or Array	Method-Ology	Ref.
	GHz		pW/ $\sqrt{\text{Hz}}$	V/W			
GaN HEMT	140	Nano-antenna	0.58	15.5 k	Single	III **	[89]
DGG-HEMT, InAlAs/ InGaAs/InP	200	Grating coupling	0.48	22.7	Single	III *	[83]
GaAs HEMT	271, 632	-	135, 1250	42, 1.6	Single	II	[42]
AlGaN/GaN SSD	300	-	280	100	Array	VI	[75]
GaAs HEMT	300	Dipole	9.1	8.5 k	Single	III ‡	[82]
GaAs/AlGaAs FET	305	-	1330	11	Single	VI	[76]
AlGaN/GaN HEMT	490–645	Bow-tie + Si lens	25–31	104 [mA/W]	Single	VI	[72]
InGaAs/AlGaAs HFET	592	Bow-tie + Si lens	500	20	Single	III	[56]
AlGaAs/GaAs HEMT	600	Log-spiral + Si lens	250	20–40 [mA/W]	Single	VI	[90]
AlGaN/GaN HEMT	700–925	Assym. dipole + Si lens	30	-	Single	III †	[91]
AlGaN/GaN HEMT	897	Assym. dipole	40	3.6 k	Single	III †	[57]
AlGaN/GaN HEMT	900	Bow-tie + Si lens	57	48 [mA/W]	Single	VI	[74]
DGG-HEMT, InAlAs/InGaAs/InP	1000	Grating coupling	15	2.2 k	Single	III *	[55]
InGaAs/GaAs	1630	-	1×10^5	170	Single	VI	[79]

* Normalised to subwavelength dimensions of 20×20 μm^2. † The area of 200×200 μm^2 is stated only in Ref. [57]. ‡ Normalised to the physical area of metal in the antenna. ** Normalised to subwavelength dimensions of 15×35 μm^2.

Table 4. Summary of reports on THz detectors employing novel low-dimensional materials.

Technology	Freq.	Antenna	Min. NEP	Responsivity	Single or Array	Method-Ology *	Ref.
	GHz		pW/ $\sqrt{\text{Hz}}$	V/W			
GFET	130–450	logarithmic spiral	600	20	Single	VI	[77]
BL-GFET	290–380	–	2000	1.2	Single	IV	[59]
BP-based FET	300	Bow-tie	1×10^4	-	Single	IV	[63]
BP-based FET	300	Bow-tie	4×10^4	0.15	Single	IV	[65]
DGG-GFET	300	-	9×10^5	-	Single	IV	[60]
Graphene Ballistic Rectifier	300	Bow-tie	34	764	Single	V	[28]
Nanowire-FET	300	Bow-tie	2.5×10^3	1.5	Single	IV	[62]
Nanowire-FET	300	Bow-tie	1000	100	Single	IV	[64]
SL-GFET, BL-GFET	300	a log-periodic circular-toothed	2×10^5 (SLG) 3×10^4 (BLG)	-	Single	IV	[61]
GFET	400	Bow-tie	130	74	Single	VI	[71]
GFET	487	Bow-tie	3000	2	Single	VI	[92]
GFET	600	Bow-tie	515	14	Single	VI	[29]
Graphene	2000	Bow-tie	15×10^4	-	Array	VI	[78]
GFET	2800	Bow-tie	160	-	Single	IV	[31]

* See definitions given at the Table 1.

The presented tables allow for the observation that directivity simulations or measurements have been mostly reported for the devices implemented in silicon material systems, which benefit from the most developed fabrication techniques. Reports on detectors which utilise novel low-dimensional materials, in most cases, used the diffraction-spot limited definition to estimate the effective area. The spread of methods used for devices fabricated using III–V materials is also significant. However, there have been reports on the non-scaled optical performance for all systems, clearly demonstrating that the performance of III–V devices is on par with that of silicon devices, while novel materials are also closely approaching state-of-the-art sensitivities.

In the following section, we present a model case for antenna-coupled detector characterisation, which illustrates the challenges arising with regards to choosing the most appropriate method for the performance evaluation. Our experimental characterisation results are compared with the device modelling predictions, allowing the reader to draw independent conclusions.

3. Samples and Measurement Setup

3.1. Detector Array Design

For the experimental part of this study, we implemented a 2 × 7 array of devices with an identical rectangular microstrip antenna (see Figure 1). Each detector is a patch antenna-coupled N-channel FET fabricated using commercial 65 nm CMOS technology with 9 metal layers (the TSMC foundry, Taiwan). The antenna was implemented in the top metal layer, with dimensions of 110 × 110 µm. The ground plane was formed by combining metallic sheets of the two lowest metal layers. A stack of metals and dielectric layers was formed on top of a slightly conductive silicon substrate (resistivity: 10 Ohm·cm) with a thickness of 279 µm and relative permittivity of 11.9.

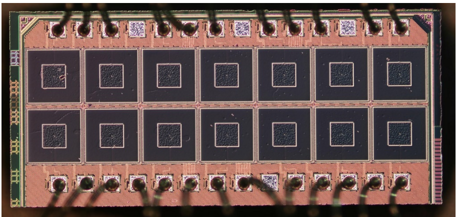

Figure 1. Micrograph photo of the die with detector array (the pitch in both directions is 279 µm).

Each detector was surrounded by a 6 µm-wide conductive metal wall, formed by all-metal layers and vias between them. The dimensions of the metal cup were 254 × 254 µm. More design details and the principal layout schematic can be found in Reference [19]. In total, we implemented 14 detectors with vertical and horizontal pitch of 279 µm, code-named from C_1 to C_{14}. All devices, located in one row and relevant to this study, employed transistors with the same 450 nm gate width while having individual gate lengths: 60 nm, 80 nm, 100 nm, 120 nm, 150 nm, 200 nm, and 240 nm, with assigned names C_8 to C_{14}. The die, which contained detectors, was packaged using a standard dual-in-line package (DIL) with 40 pins.

3.2. THz Characterisation Setup

The experimental schematics employed to characterise the detector frequency and angular response characteristics are presented in Figure 2a. It consisted of a continuous-wave terahertz spectrometer (TeraScan 1550 platform, Toptica [93,94]), which was used as the tunable source for THz radiation. The THz beam was generated by a photomixer, which was excited with two fiber-coupled distributed-feedback diode lasers (*Laser 1* and *Laser 2*), operating around 1.5 µm with a slight difference of individual emission wavelengths. The radiations of both lasers were combined using a 50:50 fiber coupler and converted to the THz frequency range by a self-complementary broadband antenna placed on an InGaAs wafer and employing an electron-hole recombination process [95]. The frequency of the generated THz signal was equal to the laser heterodyne frequency or "beat" [95,96]. The generated signal could be tuned in a wide frequency range, by controlling the temperature and current of both lasers.

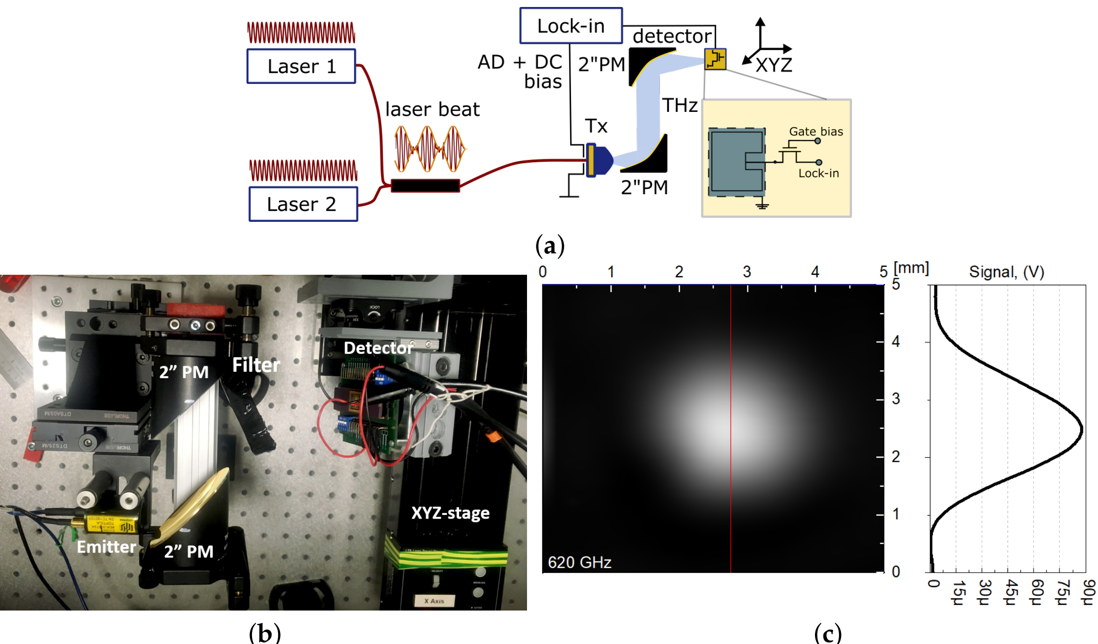

Figure 2. (**a**) Schematic building blocks and (**b**) photo of a CW THz characterisation system; (**c**) 2D scan of beam intensity at a detector location for 620 GHz.

We used a set of lasers that allowed for tuning of the photomixer emitted radiation within the frequency band of 100–1200 GHz, with a total output power of 123 µW and 1.25 µW, respectively. The THz radiation was focused on the detectory using two off-axis parabolic mirrors with focal lengths of 2″ and 4″, as shown in Figure 2b.

The incoming THz radiation had a linear polarisation with Gaussian intensity distribution perpendicular to the detector surface, as shown in Figure 2c. The radiation power level was measured using a calibrated pyroelectric detector [2] with an active area diameter of 20 mm^2 placed at the detector plane. The resolution of the beam scan was 0.1 × 0.1 mm^2. The intensity I_0 in the centre of the focal spot can be estimated from the total power, P_0, as $I_0 = 2P_0/(\pi w_0^2)$. Here, w_0 is the radius of the beam taken, concerning the P_0/e^2 level, where $w_0 = W_{\mathrm{FWHM}}/\sqrt{2\ln 2}$, with W_{FWHM} being the full width at half maximum. According to the measurement, the radiation beam's diameter at the half-power (–3 dB) point was 1.6 mm (see Figure 2c).

The transistor gate should be biased by a constant potential, in order to set it to the desired work point. An off-chip voltage supply typically provides this, through a bonding wire, pad, and on-chip bus line, which is common for all detectors on one chip. The transistor drain's output signal was registered using a lock-in amplifier synchronised with the radiation source. The lock-in amplifier (Signal Recovery 7270) had a nominal voltage input noise level of 5 nV/$\sqrt{\mathrm{Hz}}$ at 1 kHz, for an input impedance of 10 MΩ. In our measurement setup, the final noise level did not exceed 360 nV at a modulation of 1 kHz. The XYZ motorised linear stages allowed us to tune the detector's positioning and analyse the radiation beam distribution.

The left vertical axis of Figure 3 shows the signal-to-noise ratio (SNR) as a function of frequency in power decibels (i.e., $10 \cdot \log_{10}$ SNR), while the right vertical axis of the figure represents the integrated power in the radiation beam. The device C_{11} demonstrated an SNR better than 50 dB with integration time of 100 ms the maximum at 620 GHz for a total power of 7.5 µW in the beam. The "dip" near 557 GHz is the H_2O absorption line [97]. The gate was biased to an optimal position of 0.5 V; details of operating point selection are provided in Sections 4.1 and 5.2.

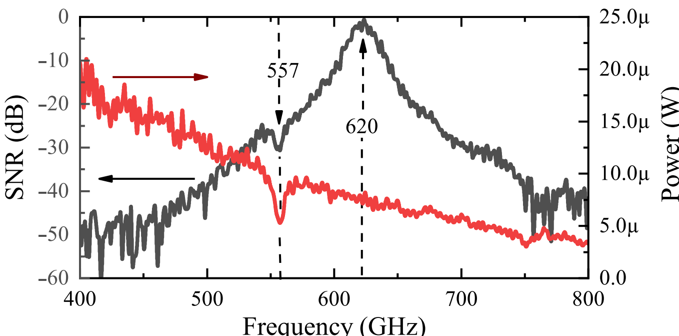

Figure 3. The black line shows the signal-to-noise ratio (**left** axis) in decibels of power (i.e., $10 \cdot \log_{10}$ SNR) for the detector C_{11} as a function of frequency. The red line shows the integrated power of the THz radiation source (**right** axis).

4. Modelling

4.1. Circuit Level Modelling of Detector

The modelling of high-frequency signal rectification with FET was performed using the standard transistor model provided by the TSMC foundry and implemented in a circuit simulator, which allowed for harmonic balance analysis. According to the implemented solution, the role of the integrated patch antenna was accounted for by introducing an equivalent power source between the FET source terminal and the ground. This power source had an impedance equal to that of the simulated antenna impedance Z_A and the power resulting from the product of half of the impinging power, P_0, and simulated antenna efficiency η_a and η_s, as shown in Figure 4a, where η_s accounts for the absorption efficiency of the receiving antenna. Its value was not simulated but, instead, we used a factor of 0.5, which is typical for half-wavelength dipole antennas [98]; however, depending on the antenna implementation, it may be close to 1 [98,99]. The detector circuit can be operated either in voltage or current readout mode.

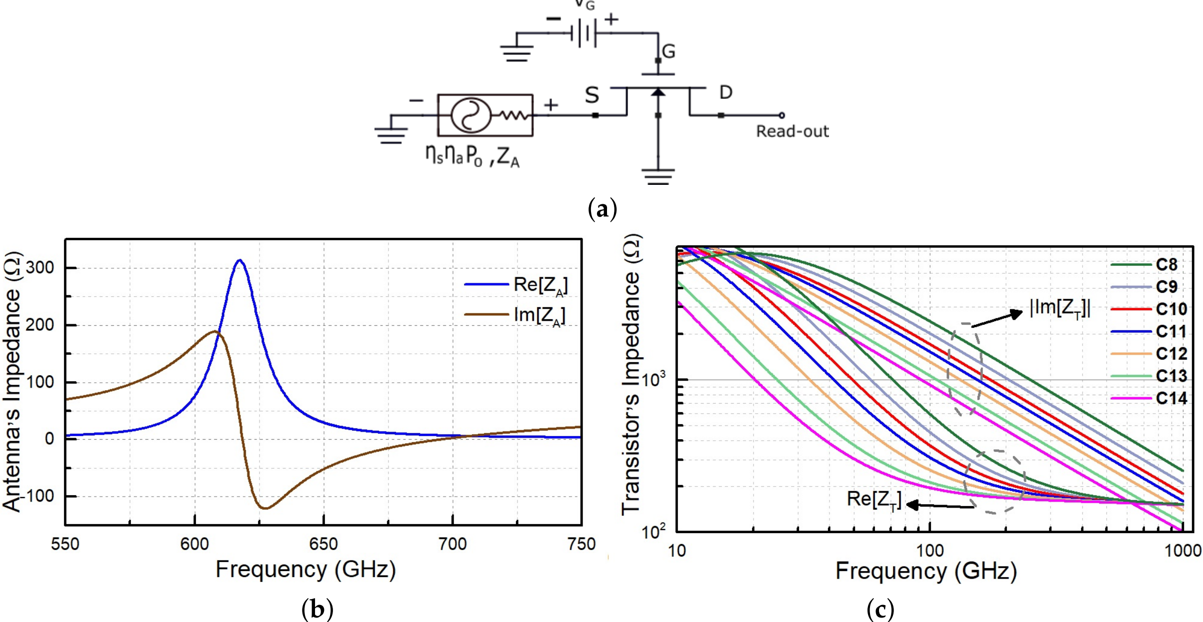

Figure 4. (**a**) Equivalent circuit of field-effect-transistor based detector; (**b**) Simulated patch antenna's impedance, Z_A, versus frequency for C_{11}; and (**c**) Real and imaginary parts of simulated transistor's impedance, Z_T, versus frequency for the gate bias corresponding to the optimum operation point for C_8–C_{14}.

As detector modelling requires emulating the antenna as an equivalent power source, in order to account for simulation-relevant antenna characteristics, we employed the princi-

ple of reciprocity and performed electromagnetic simulations using the finite-difference time-domain method. The results of these simulations are presented, in detail, in the following section. All selected antennas had a typical radiation efficiency value, η_a, of about 0.5 at 620 GHz. The simulation results for the impedance of antennas and transistors, Z_T, are shown in Figure 4b,c, respectively. All antennas had very similar impedance characteristics, with variations being lower than 4 Ω. The detector C_{14} had the best impedance, when matched to the antenna impedance at 620 GHz (close to 1.0); however, the more considerable capacitive contribution of detector C_8 also resulted in a good matching factor (close to 0.5; compare the simulated impedance values at 620 GHz in Figure 4b,c).

We should note that, for precise performance evaluation of a terahertz detector, it is necessary to estimate the impinging power, P_0, which requires the knowledge of the experimentally measurable intensity distribution and the effective area of the receiving antenna. The latter can be experimentally estimated from angular antenna response characteristics or can be deduced from simulations.

4.2. Electromagnetic Simulations of Antenna

We decided on microstrip patch antennas for this study. This type of antenna belongs to a well-studied antenna class and has good, predictable radiation properties under front-side illumination. Detectors have been implemented using a similar approach, as detailed in Reference [19]. The patch antenna was implemented in the top metal layer of the CMOS technological process, with dimensions of 110 × 110 µm (see insert in Figure 2a). We applied the finite element method with an adaptive mesh using the CST Studio Suite software, in order to model the investigated antenna structures and evaluate the electromagnetic field's far-field distributions.

One of the distinctive properties of patch antennas with ground planes is that the lower metal planes allow for efficient suppression of radiation propagation into the thick dielectric substrate. The impact of radiation propagating in the substrate has been addressed in many works which reported about the dependencies of antenna parameters on the substrate thickness [100] and the detector's position on the substrate [101,102]. Although such a phenomenon can be deliberately used to increase the antenna directivity, it might challenge estimation of the antenna's effective area. However, the effect may even be used to boost the efficiency of a detector, such as in [46]. To clarify the role of radiation leaking into the substrate in our devices, we investigated two cases numerically. As a metric, we used D, the antenna's directivity, which was used to determine the device sensitivity. The first case was a single device on a finite-size dielectric substrate. The second case corresponded to an exact device model with a double line array having 14 detector elements with identical parameters and a pitch of 279 µm, as shown in Figure 5.

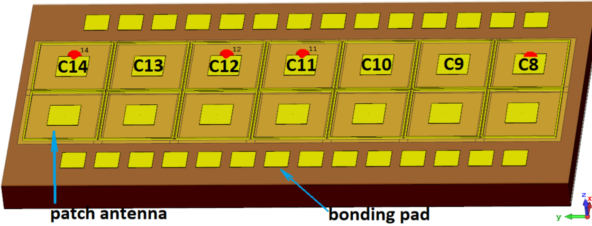

Figure 5. A 3D model of a die with a 2 × 7 array of identical antennas and contact pads on a Si substrate.

The far-field radiation analysis in the performed simulations demonstrated a difference in the maximum amplitude of the main lobes. In the case of a single device, the main lobe's amplitude was D = 6 dBi, with an angular width of 89°, and the radiation direction was perpendicular to the surface. In the array arrangement, we simulated an increase in directivity, to 8.65 dBi for the device on the die edge and 8.45 dBi for devices in the chip's middle, as shown in Figure 6a. The resulting angular widths were 89° and 95°, and the

main lobe had a shift of 12° and 9°, respectively. Other devices in the middle part of the chip had the same difference as those near the edges.

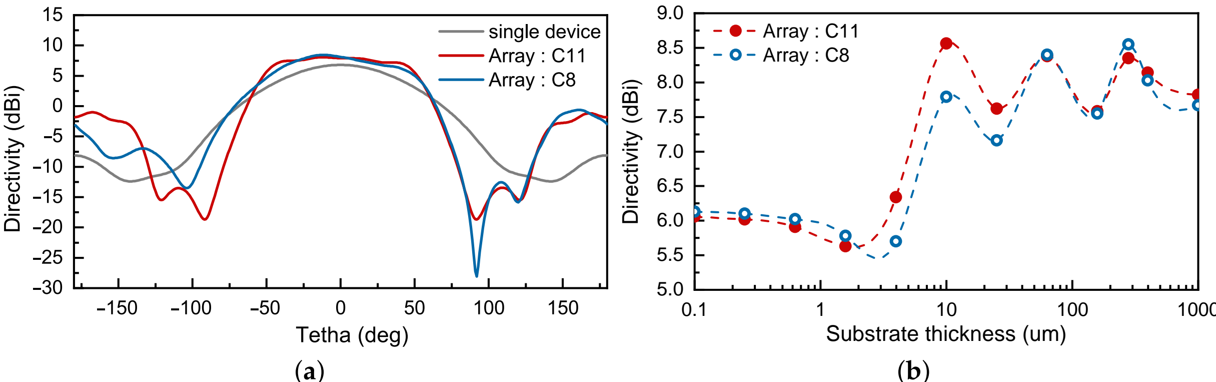

Figure 6. (**a**) Comparison of radiation patterns in the E-plane for a single-chip device (grey line) and a device integrated into the array. The blue line corresponds to a detector positioned in the middle of the array line (C_{11}), while the red line is for the device placed at the side (C_8). The result is presented for 620 GHz; (**b**) Directivity as a function of substrate thickness for the device in the middle of the array (red line) and at the side position (blue line).

Figure 6b presents the results of directivity modelling for two detector array elements with substrate thicknesses ranging from 0.1 µm up to 1 mm. Decreasing the substrate thickness demonstrated the relatively stable value of the device's directivity in the middle part of the slab, as the edge device.

5. Experimental Results

5.1. Methodology of Measuring Device's Effective Area and Determining Input Power

The performance of an antenna-coupled THz detector can be presented in several different ways. One of the traceable detector-related metrics is its cross-sectional responsivity, which only considers the amount of power impinging on to the antenna's effective area, A_{eff}. The effective area, A_{eff}, can be considered in several different ways, which were previously discussed and summarised in Table 1.

We applied a standard methodology for the characterisation of receiving antennas and derived the effective area from the detector's directivity. The directivity was determined by recording the rectified voltage as a function of tilt angles of the devices in the E- and H-planes. The radiation patterns measured at 620 GHz in these two projections are shown in Figure 7. As can be seen from the figure, for C_9–C_{11} we had an almost 10-degree shift in the angle of maximal gain, which indicates that part of the radiation propagated through the surface or the substrate. The maximal gain angle remained untilted in test simulations for a single antenna with symmetric background and without substrate.

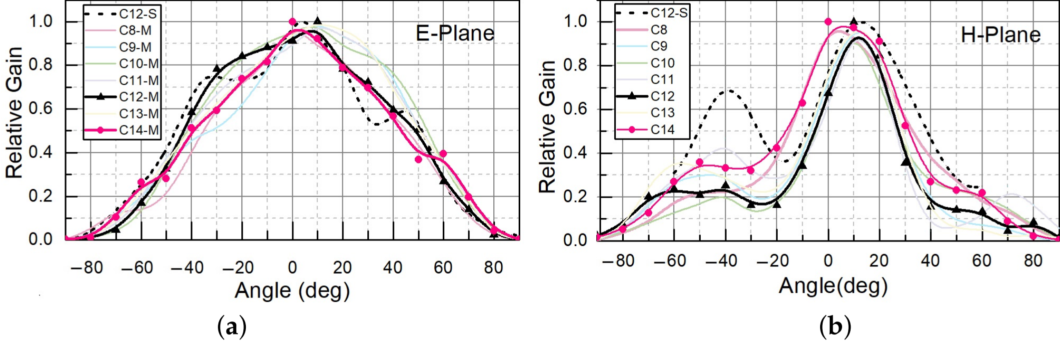

Figure 7. Dependency of the THz response of C_8–C_{14} for various (**a**) E-plane and (**b**) H-plane tilt angles at 620 GHz. The simulated response of C_{12} is displayed with a dotted line.

A summary of the experimental results for devices C_8–C_{14} is presented in Figure 7. For comparison, the modelled antenna's radiation patterns for the central device C_{12} in the E- and H-planes are shown as a dashed line in the same figure. As can be seen, the patterns for C_9–C_{13} were similar to each other. Patterns C_8 and C_{14} had a slightly lower shift of maximum direction in the E-plane. The simulation results for C_{12} were in good agreement with the measured pattern.

Table 5 gives the experimentally determined FWHM angles for C_8–C_{14} at 620 GHz. The maximum directivity can be evaluated after extracting the values of FWHM angles Θ_E and Θ_H, employing the expression for the directivity D in the approximation for small-angle values: $D \approx 72815/(\Theta_H^2 + \Theta_E^2)$ (for more details, see [48], p. 54). We can use D for estimation of A_{eff}, as shown in the remarks for method II in Table 1. We note the excellent quantitative agreement at 620 GHz between the directivity values estimated with this equation and those obtained from the experimental data. The simulations were also performed for a single detector. We obtained a directivity of 6 dBi, giving an effective area of 0.074 mm^2, which was quite close to the chosen pitch area (0.076 mm^2).

As shown in Table 5, the calculated effective area for detectors placed in an array resulted in slightly larger values than for a single detector. We also measured the dependency of the response for one detector (C_8, which was the most sensitive one, due to the shortest gate length) at different frequencies of incoming THz radiation (590–660 GHz) in both the E- and H-planes. The results are shown in Figure 8. As can be seen from the figure, the angle of maximum gain for C_8 at different frequencies varied, implying the existence of propagating substrate waves.

Table 5. Summary of the directivity measurements and simulation.

Detector	Θ_E (deg)	Θ_H (deg)	D Meas. (dBi)	A_{eff} Meas. (mm^2)	D Sim. (dBi)	A_{eff} Sim. (mm^2)
C_8	87	47	8.70	0.138	8.65	0.136
C_9	93	38	8.58	0.134	8.43	0.130
C_{10}	94	35	8.59	0.134	8.65	0.136
C_{11}	93	32	8.76	0.140	8.45	0.130
C_{12}	93	36	8.60	0.136	8.73	0.139
C_{13}	90	38	8.82	0.142	8.59	0.134
C_{14}	85	46	8.90	0.145	7.83	0.113

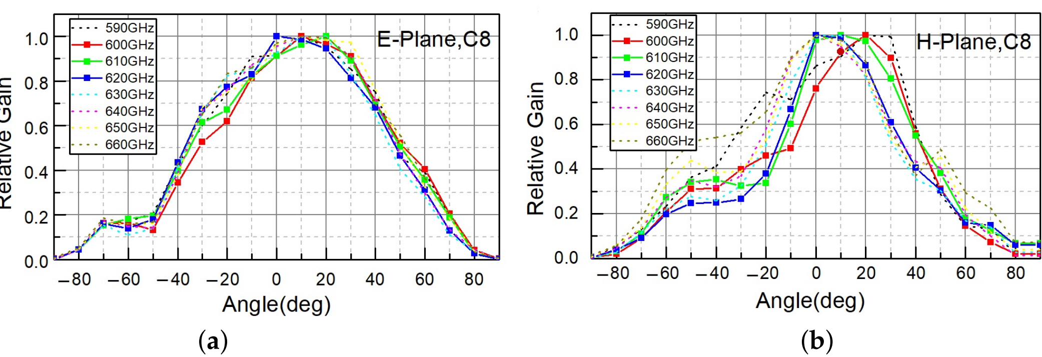

Figure 8. Dependency of the THz response of C_8 on (**a**) E-plane and (**b**) H-plane tilt angles for different incoming THz radiation frequencies.

With the detector effective area values estimated through the simulated and presented experiments, we then obtained estimates for the impinging power within the effective antenna cross-section, using $P_{in} = I_0 \cdot A_{\text{eff}}$.

5.2. Terahertz Responsivity

Figure 9 shows the measured cross-sectional voltage $\Re_{V,c}$ (left) and current responsivity $\Re_{I,c}$ (right), together with simulation results (dash line) obtained with the TSMC 65 nm model from the process technology provider. Using an experimentally defined effective area, we obtained a maximum cross-section voltage responsivity of 1414 V/W for C_8 at a gate bias voltage of V_G 0.35 V, which was below the device's threshold voltage. The peak of current responsivity was 66 mA/W, corresponding to a V_G of 0.65 V. As can be seen, a good correlation between the simulation and measurement results was obtained. The slight difference between the foundry model-predicted responsivity and experimental data could be attributed to the slight scattering of individual device parameters, whereas the simulation was performed using an average representative. For comparison, we also present the estimation of cross-section responsivity expected for a single detector with D = 6 dBi, under substrate wave suppression. As can be seen in Figure 9, the value may become about 2 times larger than the measured responsivity; however, this would exceed the modelled value. The comparison, thus, underlines the necessity of thorough analysis of array performance, instead of using simplified assumptions such as assuming the area to be defined by the pitch or the effective area of the idealised patch without the manifestation of substrate waves.

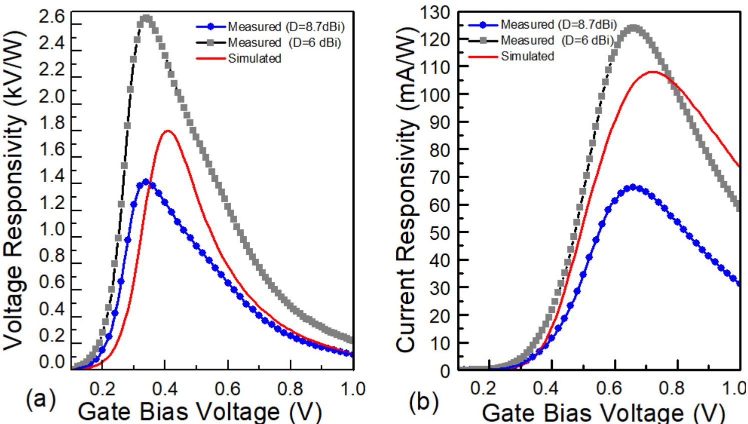

Figure 9. Voltage (**a**) and current (**b**) responsivity of C_8 vs. gate voltage bias at 620 GHz. Two different directivity values were used for the responsivity estimation: D = 6 dBi (the detector treated as a single one, the gray line) and D = 8.7 dBi (treated as a part of an array, the blue line). The red line shows the simulation results obtained with the TSMC 65 nm model.

The used figure-of-merit, which defines the detector's sensitivity, was the NEP. This is defined as the input power that results in a signal-to-noise ratio of one for the equivalent noise bandwidth of 1 Hz. One can calculate the cross-sectional NEP of the transistor, according to $\text{NEP} = N_V/\Re_{V,c}$, where N_V is the noise voltage spectral density of the detector (or, $\text{NEP} = N_I/\Re_{I,c}$, where N_I is the noise current spectral density of the detector). As the detection was studied under zero drain bias, thermal noise was the only source of noise for the transistor, which can be calculated by $N_V = \sqrt{4k_B T R_{DC}}$, where k_B is the Boltzmann constant, T is the temperature, and R_{DC} is the DC drain-source resistance of the transistor. This statement has been tested on many different devices of the same kind and has been addressed in a series of reports [24,25,103].

The measured and simulated NEP values of C_8 under different gate bias conditions at a radiation frequency of 620 GHz are plotted in Figure 10. The minimum measured cross-sectional NEP was 19.2 pW/$\sqrt{\text{Hz}}$, corresponding to a V_G of 0.59 V. However, this value can get as low as 10 pW/$\sqrt{\text{Hz}}$ assuming D = 6 dBi, which was even slightly below the predictions by simulations, which are presented with a red line. A minimum simulated value of 13.4 pW/$\sqrt{\text{Hz}}$ at a V_G of 0.55 V was obtained. Therefore, we can conclude that our estimated performance values well-matched those predicted by the simulations, supporting

the directivity-related estimation of the effective area. It is important to note that the only assumptions we used in model simulations were related to the antenna efficiency factors, and only these were taken from the results of the antenna's electrodynamic modelling. The slight differences in the shapes of the curves might have originated from the fact that the simulation model described statistically averaged device characteristics, whereas the experiments were performed using individual devices.

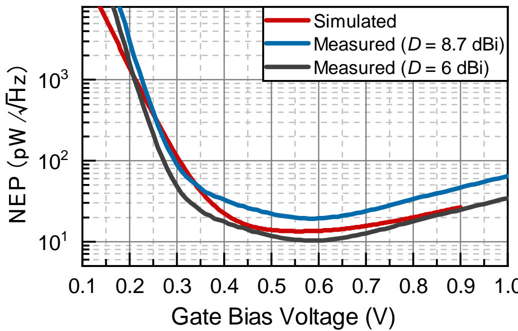

Figure 10. Noise equivalent power of C_8 as a function of the gate voltage bias.

Table 6 compares the performance of 65 nm CMOS detectors, considering the different methods used to calculate the effective area. As one can see from the table, considering the effective area to be equal to the physical area (pitch between devices) or as the area of the diffraction-limited spot resulted in a smaller estimated effective area, compared to the experimental estimate and led to about two-fold overestimation of the performance of the sensor (i.e., increasing in the responsivity or decreasing in the value of NEP). Due to the selection of focusing mirrors, the optical performance (presented in the last line) was about 20-fold lower than the cross-sectional performance. The main reason for this lies in the used optics, with much lower numerical aperture, which did not match the antenna's angular radiation characteristics. Nevertheless, another conclusion can be drawn, regarding the meaning of 2.5 pW/$\sqrt{\text{Hz}}$, which would result as the NEP for the omnidirectional antenna case. As it was not efficiently de-embedded and was much lower than the expected value from our simulations (of 13.4 pW/$\sqrt{\text{Hz}}$), as expected without any assumption of area, it has no direct relevance to either the electrical or optical performance of the devices, besides being embedded again with the directivity value.

Table 6. Comparison of responsivity and NEP of the detector, considering different methods calculating the effective area.

Method	A_{eff} (mm^2)	Max. Responsivity (V/W)	Min.NEP (pW/$\sqrt{\text{Hz}}$)
Measured directivity of the detector in array D = 8.7 dBi)	0.138	1414	19.2
Simulated directivity of single detector D = 6 dBi	0.074	2651	10.28
Physical area defined by the pitch between devices	0.077	2545	10.7
Area of diffraction limited spot	0.058	3368	8.09
From the antenna gain ($G = \eta_a \cdot D$)	0.069	2828	9.6
Normalised for the omnidirectional antenna case	0.018	10.8 K	2.5
Without any normalisation (Optical performance)		63.6	428

6. Conclusions

In this paper, we presented a review of the methods currently in use for the characterisation of antenna-coupled field-effect transistor-based THz detectors. We showed that at least six primary characterisation methods are commonly applied. While all of these methods are valid in the range of their applicability, in most cases, it can become challenging to select a correct method without performing thorough experimental characterisation,

which is required to assess the effective area of the detector. We present a comprehensive study of field-effect transistor-based antenna-coupled detectors at a frequency of 620 GHz, in order to illustrate the ambiguities arising in practical cases. Based on numerical simulations, supported by experimental characterisations of the angular response dependence, we showed that the detector's effective area in a small array can become considerably larger than that defined by the pitch between devices or when considering a single device. For the resonant frequency of 620 GHz and by considering the maximum directivity-defined effective area, we arrived at a room-temperature cross-sectional noise-equivalent power of 19.2 $\mathrm{pW}/\sqrt{\mathrm{Hz}}$. In contrast, for the omnidirectional antenna, this value was reported as low as 2.5 $\mathrm{pW}/\sqrt{\mathrm{Hz}}$; however, the latter value was not directly linked with either the optimal or achievable performance and, for the concomitant system, the analysis should be re-embedded with the measured directivity value of 8.7 dBi. This example shows how, by mixing between methodologies, one can manipulate the NEP to one order of magnitude in overestimating the detector's performance and seemingly breaking the 10 $\mathrm{pW}/\sqrt{\mathrm{Hz}}$ barrier.

Finally, we wish to summarise that, when comparing the performance of different devices or novel detection methods, the evaluation method used should be based on the directivity (or by any other technique with a traceable assessment of the effective sensor area). The presented results detailed sensitivity classification methods paving the way towards the unified scientific metrology of FET-based THz sensors, which is important for both researchers competing for records as well as potential users and engineers who intend to utilise the sensors to construct future THz systems.

Author Contributions: Conceptualisation, A.L.; methodology, A.L. and D.B.B.; software, E.J., D.B.B., and A.L.; validation, E.J., D.B.B., and A.L.; formal analysis, J.Z., E.J., D.B.B. and A.L.; investigation, J.Z., E.J. and D.B.B.; data curation, K.I.; writing—original draft preparation, E.J. and D.B.B.; writing—review and editing, K.I., A.L. and W.K.; visualisation, E.J., D.B.B. and K.I.; supervision, A.L.; project administration, A.L. and W.K.; funding acquisition, A.L. and W.K. All authors have read and agreed to the published version of the manuscript.

Funding: The work was partially supported by the "International Research Agendas" program of the Foundation for Polish Science co-financed by the European Union under the European Regional Development Fund (No. MAB/2018/9) for CENTERA. The research was also partially supported by the Foundation for Polish Science through the TEAM project PIOR.04.04.00-00-3D76/16(TEAM/2016-3/25); and by the ESA, grant number 4000122246/17NL/SC.

Institutional Review Board Statement: Not applicable.

Informed Consent Statement: Not applicable.

Data Availability Statement: The data that support the findings of this study are available from the corresponding author (E.J.) upon reasonable request.

Conflicts of Interest: The authors declare no conflict of interest. The funders had no role in the design of the study; in the collection, analyses, or interpretation of data; in the writing of the manuscript; or in the decision to publish the results.

Abbreviations

The following abbreviations are used in this manuscript:

III–V	III–V compound semiconductor
BiCMOS	Bipolar CMOS
BL-GFET	Bi-layer graphene field-effect transistor
BLG	Bi-layer GFET (see BL-GFET)
BP-based FET	Black phosphorus-based field-effect transistor
CAD	Computer-aided design
CMOS	Complementary metal–oxide–semiconductor
CSDRA	Chip scale dielectric resonator antenna
DGG-HEMT	Dual-grating-gate high-electron-mobility transistor
DGG-GFET	Dual-grating-gate graphene field-effect transistor

FD-SOI	Fully depleted silicon on insulator
FDTD	Finite-difference time-domain
FET	Field-effect transistor
FWHM	Full width at half maximum
GFET	Graphene field-effect transistor
HBT	Heterojunction bipolar transistor
HEMT	High-electron-mobility transistor
HFET	Heterostructure FET
MOSFET	Metal–oxide–semiconductor field-effect transistor
Nanowire-FET	Nanowire-based field-effect transistor
NEP	Noise equivalent power
P–N diode	P–N junction diode
SSD	Self-switching device
SBD	Schottky barrier diode
SL-GFET	Single-layer graphene field-effect transistor
SLG	Single-layer GFET (see SL-GFET)
SNR	Signal-to-noise ratio
SOI	Silicon on insulator
THz	Terahertz

References

1. Desmaris, V.; Rashid, H.; Pavolotsky, A.; Belitsky, V. Design, simulations and optimization of micromachined Golay-cell based THz sensors operating at room temperature. *Procedia Chem.* **2009**, *1*, 1175–1178. [CrossRef]
2. Müller, R.; Bohmeyer, W.; Kehrt, M.; Lange, K.; Monte, C.; Steiger, A. Novel Detectors for Traceable THz Power Measurements. *J. Infrared, Millim. Terahertz Waves* **2014**, *35*, 659–670. [CrossRef]
3. Simoens, F.; Meilhan, J. Terahertz real-time imaging uncooled array based on antenna- and cavity-coupled bolometers. *Philos. Trans. R. Soc. A Math. Phys. Eng. Sci.* **2014**, *372*, 20130111. [CrossRef]
4. Brown, E.R.; Young, A.C.; Zimmerman, J.; Kazerni, H.; Gossard, A.C. Advances in Schottky rectifier performance. *IEEE Microw. Mag.* **2007**, *8*, 54–59. [CrossRef]
5. Hesler, J.L.; Crowe, T.W. Responsivity and noise measurements of zero-bias Schottky diode detectors. In Proceedings of 18th International Symposium Space Terahertz Technology (ISSTT 2007), Pasadena, CA, USA, 21–23 March 2007; pp. 89–92.
6. Sydlo, C.; Cojocari, O.; Schçnherr, D.; Goebel, T.; Meissner, P.; Hartnagel, H. Fast THz detectors based on InGaAs Schottky diodes. *Frequenz* **2008**, *62*, 107–110. [CrossRef]
7. Al Hadi, R.; Sherry, H.; Grzyb, J.; Zhao, Y.; Forster, W.; Keller, H.M.; Cathelin, A.; Kaiser, A.; Pfeiffer, U.R. A 1 k-Pixel Video Camera for 0.7–1.1 Terahertz Imaging Applications in 65-nm CMOS. *IEEE J. Solid-State Circuits* **2012**, *47*, 2999–3012. [CrossRef]
8. Lisauskas, A.; Bauer, M.; Boppel, S.; Mundt, M.; Khamaisi, B.; Socher, E.; Venckevičius, R.; Minkevičius, L.; Kašalynas, I.; Seliuta, D.; et al. Exploration of Terahertz Imaging with Silicon MOSFETs. *J. Infrared Millim. Terahertz Waves* **2014**, *35*, 63–80. [CrossRef]
9. Boukhayma, A.; Dupret, A.; Rostaing, J.P.; Enz, C. A low-noise CMOS THz imager based on source modulation and an in-pixel high-Q passive switched-capacitor N-path filter. *Sensors* **2016**, *16*, 325. [CrossRef]
10. Zdanevičius, J.; Bauer, M.; Boppel, S.; Palenskis, V.; Lisauskas, A.; Krozer, V.; Roskos, H.G. Camera for High-Speed THz Imaging. *J. Infrared Millim. Terahertz Waves* **2015**, *36*, 986–997. [CrossRef]
11. Yokoyama, S.; Ikebe, M.; Kanazawa, Y.; Ikegami, T.; Ambalathankandy, P.; Hiramatsu, S.; Sano, E.; Takida, Y.; Minamide, H. 5.8 a 32 × 32-Pixel 0.9 THz Imager with Pixel-Parallel 12b VCO-Based ADC in 0.18 µm CMOS. In Proceedings of the 2019 IEEE International Solid- State Circuits Conference—(ISSCC), San Francisco, CA, USA, 17–21 February 2019; pp. 108–110. [CrossRef]
12. Knap, W.; Kachorovskii, V.; Deng, Y.; Rumyantsev, S.; Lü, J.Q.; Gaska, R.; Shur, M.S.; Simin, G.; Hu, X.; Khan, M.A.; et al. Nonresonant detection of terahertz radiation in field effect transistors. *J. Appl. Phys.* **2002**, *91*, 9346. [CrossRef]
13. Knap, W.; Teppe, F.; Meziani, Y.M.; Dyakonova, N.; Lusakowski, J.; Boeuf, F.; Skotnicki, T.; Maude, D.K.; Rumyantsev, S.; Shur, M.S. Plasma wave detection of sub-terahertz and terahertz radiation by silicon field-effect transistors. *Appl. Phys. Lett.* **2004**, *85*, 675. [CrossRef]
14. Lisauskas, A.; Pfeiffer, U.; Öjefors, E.; Bolìvar, P.H.; Glaab, D.; Roskos, H.G. Rational design of high-responsivity detectors of terahertz radiation based on distributed self-mixing in silicon field-effect transistors. *J. Appl. Phys.* **2009**, *105*, 114511. [CrossRef]
15. Dyakonov, M.I. Generation and detection of Terahertz radiation by field effect transistors. *Comptes Rendus Phys.* **2010**, *11*, 413–420. [CrossRef]
16. Preu, S.; Kim, S.; Verma, R.; Burke, P.G.; Sherwin, M.S.; Gossard, A.C. An improved model for non-resonant terahertz detection in field-effect transistors. *J. Appl. Phys.* **2012**, *111*, 024502. [CrossRef]

17. Boppel, S.; Lisauskas, A.; Mundt, M.; Seliuta, D.; Minkevičius, L.; Kašalynas, I.; Valusis, G.; Mittendorff, M.; Winnerl, S.; Krozer, V.; et al. CMOS Integrated Antenna-Coupled Field-Effect Transistors for the Detection of Radiation From 0.2 to 4.3 THz. *IEEE Trans. Microw. Theory Tech.* **2012**, *60*, 3834–3843. [CrossRef]
18. Rudin, S.; Rupper, G.; Gutin, A.; Shur, M. Theory and measurement of plasmonic terahertz detector response to large signals. *J. Appl. Phys.* **2014**, *115*, 064503. [CrossRef]
19. Zdanevičius, J.; Čibiraitė, D.; Ikamas, K.; Bauer, M.; Matukas, J.; Lisauskas, A.; Richter, H.; Hagelschuer, T.; Krozer, V.; Hübers, H.; et al. Field-Effect Transistor Based Detectors for Power Monitoring of THz Quantum Cascade Lasers. *IEEE Trans. Terahertz Sci. Technol.* **2018**, *8*, 613–621. [CrossRef]
20. Lu, J.Q.; Shur, M.; Hesler, J.; Sun, L.; Weikle, R. Terahertz detector utilizing two-dimensional electronic fluid. *IEEE Electron Device Lett.* **1998**, *19*, 373–375. [CrossRef]
21. Tauk, R.; Teppe, F.; Boubanga, S.; Coquillat, D.; Knap, W.; Meziani, Y.M.; Gallon, C.; Boeuf, F.; Skotnicki, T.; Fenouillet-Beranger, C.; et al. Plasma wave detection of terahertz radiation by silicon field effects transistors: Responsivity and noise equivalent power. *Appl. Phys. Lett.* **2006**, *89*, 253511. [CrossRef]
22. Javadi, E.; Lisauskas, A.; Shahabadi, M.; Masoumi, N.; Zhang, J.; Matukas, J.; Roskos, H.G. Terahertz Detection With a Low-Cost Packaged GaAs High-Electron-Mobility Transistor. *IEEE Trans. Terahertz Sci. Technol.* **2019**, *9*, 27–37. [CrossRef]
23. Öjefors, E.; Baktash, N.; Zhao, Y.; Hadi, R.A.; Sherry, H.; Pfeiffer, U.R. Terahertz imaging detectors in a 65-nm CMOS SOI technology. In Proceedings of the 2010 Proceedings of ESSCIRC, Seville, Spain, 14–16 September 2010; pp. 486–489.
24. Bauer, M.; Venckevičius, R.; Kašalynas, I.; Boppel, S.; Mundt, M.; Minkevičius, L.; Lisauskas, A.; Valušis, G.; Krozer, V.; Roskos, H.G. Antenna-coupled field-effect transistors for multi-spectral terahertz imaging up to 4.25 THz. *Opt. Express* **2014**, *22*, 19235. [CrossRef]
25. Ferreras-Mayo, M.; Čibiraitė-Lukenskienė, D.; Lisauskas, A.; Grajal, J.; Krozer, V. Broadband sensing around 1 THz via a novel biquad-antenna-coupled low-NEP detector in CMOS. *IEEE Trans. Terahertz Sci. Technol.* **2020**, *11*, 16–27. [CrossRef]
26. Ikamas, K.; Čibiraitė, D.; Lisauskas, A.; Bauer, M.; Krozer, V.; Roskos, H.G. Broadband Terahertz Power Detectors Based on 90-Nm Silicon CMOS Transistors with Flat Responsivity up to 2.2 THz. *IEEE Electron Device Lett.* **2018**, *39*. [CrossRef]
27. Virginia Diodes, Inc. VDI Zero Bias Detector Specifications. Available online: https://www.vadiodes.com/en/products/detectors (accessed on 22 February 2021).
28. Auton, G.; But, D.B.; Zhang, J.; Hill, E.; Coquillat, D.; Consejo, C.; Nouvel, P.; Knap, W.; Varani, L.; Teppe, F.; et al. Terahertz Detection and Imaging Using Graphene Ballistic Rectifiers. *Nano Lett.* **2017**, *17*, 7015–7020. [CrossRef]
29. Zak, A.; Andersson, M.A.; Bauer, M.; Matukas, J.; Lisauskas, A.; Roskos, H.G.; Stake, J. Antenna-Integrated 0.6 THz FET Direct Detectors Based on CVD Graphene. *Nano Lett.* **2014**, *14*, 5834–5838. [CrossRef]
30. Bauer, M.; Andersson, M.; Zak, A.; Sakalas, P.; Čibiraitė, D.; Lisauskas, A.; Schröter, M.; Stake, J.; Roskos, H.G. The potential for sensitivity enhancement by the thermoelectric effect in carbon-nanotube and graphene Tera-FETs. *J. Phys. Conf. Ser.* **2015**, *647*, 012004. [CrossRef]
31. Viti, L.; Purdie, D.G.; Lombardo, A.; Ferrari, A.C.; Vitiello, M.S. HBN-Encapsulated, Graphene-based, Room-temperature Terahertz Receivers, with High Speed and Low Noise. *Nano Lett.* **2020**, *20*, 3169–3177. [CrossRef]
32. Sizov, F.; Rogalski, A. THz detectors *Prog. Quantum Electron.* **2010**. [CrossRef]
33. Sizov, F. Terahertz radiation detectors: The state-of-the-art. *Semicond. Sci. Technol.* **2018**, *33*, 123001. [CrossRef]
34. Sizov, F.; Golenkov, A.; But, D.; Sakhno, M.; Reva, V. Sub-THz radiation room temperature sensitivity of long-channel silicon field effect transistors. *Opto-Electron. Rev.* **2012**, *20*, 194–199. [CrossRef]
35. Sakhno, M.; Golenkov, A.; Sizov, F. Uncooled detector challenges: Millimeter-wave and terahertz long channel field effect transistor and Schottky barrier diode detectors. *J. Appl. Phys.* **2013**, *114*, 164503. [CrossRef]
36. But, D.B.; Drexler, C.; Sakhno, M.V.; Dyakonova, N.; Drachenko, O.; Sizov, F.F.; Gutin, A.; Ganichev, S.D.; Knap, W. Nonlinear photoresponse of field effect transistors terahertz detectors at high irradiation intensities. *J. Appl. Phys.* **2014**, *115*, 164514. [CrossRef]
37. Jain, R.; Zatta, R.; Grzyb, J.; Harame, D.; Pfeiffer, U.R. A Terahertz Direct Detector in 22 nm FD-SOI CMOS. In Proceedings of the 2018 13th European Microwave Integrated Circuits Conference (EuMIC), Madrid, Spain, 23–25 September 2018; IEEE: Madrid, Spain, 2018; pp. 25–28. [CrossRef]
38. Volakis, J.L. (Ed.) *Antenna Engineering Handbook*, 4th ed.; McGraw-Hill: New York, NY, USA, 2007.
39. Al Hadi, R.; Grzyb, J.; Heinemann, B.; Pfeiffer, U.R. A Terahertz Detector Array in a SiGe HBT Technology. *IEEE J. Solid-State Circuits* **2013**, *48*, 2002–2010. [CrossRef]
40. Liu, Z.Y.; Liu, L.Y.; Yang, J.; Wu, N.J. A CMOS fully integrated 860-GHz terahertz sensor. *IEEE Trans. Terahertz Sci. Technol.* **2017**, *7*, 455–465. [CrossRef]
41. Han, R.; Zhang, Y.; Kim, Y.; Kim, D.Y.; Shichijo, H.; Afshari, E.; Kenneth, K.O. Active terahertz imaging using Schottky diodes in CMOS: Array and 860-GHz pixel. *IEEE J. Solid-State Circuits* **2013**, *48*, 2296–2308. [CrossRef]
42. Javadi, E.; Delgado-Notario, J.A.; Masoumi, N.; Shahabadi, M.; Velázquez-Pérez, J.E.; Meziani, Y.M. Continuous Wave Terahertz Sensing Using GaN HEMTs. *Phys. Status Solidi* **2018**, *215*, 1700607. [CrossRef]
43. Ahmad, Z.; Kenneth, K.O. THz Detection Using p+/n-Well Diodes Fabricated in 45-nm CMOS. *IEEE Electron Device Lett.* **2016**, *37*, 823–826. [CrossRef]

44. But, D.B.; Javadi, E.; Knap, W.; Ikamas, K.; Lisauskas, A. Silicon based resonant power detector for 620 GHz. In Proceedings of the 2020 23rd International Microwave and Radar Conference (MIKON), Warsaw, Poland, 5–8 October 2020; pp. 305–308. [CrossRef]
45. Karolyi, G.; Gergelyi, D.; Foldesy, P. Sub-THz Sensor Array With Embedded Signal Processing in 90 nm CMOS Technology. *IEEE Sens. J.* **2014**, *14*, 2432–2441. [CrossRef]
46. Shaulov, E.; Jameson, S.; Socher, E. A Zero Bias J-Band Antenna-Coupled Detector in 65-nm CMOS. *IEEE Trans. Terahertz Sci. Technol.* **2021**, *11*, 62–69. [CrossRef]
47. Fang, T.; Liu, Z.Y.; Liu, L.Y.; Li, Y.Y.; Liu, J.Q.; Liu, J.; Wu, N.J. Detection of 3.0 THz wave with a detector in 65 nm standard CMOS process. In Proceedings of the 2017 IEEE Asian Solid-State Circuits Conference (A-SSCC), Seoul, Korea, 6–8 November 2017; IEEE: Piscataway, NJ, USA, 2017; pp. 189–192. [CrossRef]
48. Balanis, C.A. *Antenna Theory: Analysis and Design*, 4th ed.; Wiley: Hoboken, NJ, USA, 2016.
49. Pfeiffer, U.; Grzyb, J.; Sherry, H.; Cathelin, A.; Kaiser, A. Toward low-NEP room-temperature THz MOSFET direct detectors in CMOS technology. In Proceedings of the 38th International Conference on Infrared, Millimeter, and Terahertz Waves (IRMMW-THz), Mainz, Germany, 1–6 September 2013; IEEE: Piscataway, NJ, USA, 2013; pp. 1–2.
50. Jain, R.; Rücker, H.; Pfeiffer, U.R. Zero gate-bias terahertz detection with an asymmetric NMOS transistor. In Proceedings of the 2016 41st International Conference on Infrared, Millimeter, and Terahertz waves (IRMMW-THz), Copenhagen, Denmark, 25–30 September 2016; IEEE: Piscataway, NJ, USA, 2016; pp. 1–2.
51. Sherry, H.; Al Hadi, R.; Grzyb, J.; Öjefors, E.; Cathelin, A.; Kaiser, A.; Pfeiffer, U.R. Lens-integrated THz imaging arrays in 65 nm CMOS technologies. In Proceedings of the 2011 IEEE Radio Frequency Integrated Circuits Symposium, Baltimore, MD, USA, 5–7 June 2011; IEEE: Piscataway, NJ, USA, 2011; pp. 1–4.
52. Kim, D.Y.; Park, S.; Han, R.; Kenneth, K. Design and demonstration of 820-GHz array using diode-connected NMOS transistors in 130-nm CMOS for active imaging. *IEEE Trans. Terahertz Sci. Technol.* **2016**, *6*, 306–317. [CrossRef]
53. Ojefors, E.; Pfeiffer, U.R.; Lisauskas, A.; Roskos, H.G. A 0.65 THz Focal-Plane Array in a Quarter-Micron CMOS Process Technology. *IEEE J. Solid-State Circuits* **2009**, *44*, 1968–1976. [CrossRef]
54. Sengupta, K.; Seo, D.; Yang, L.; Hajimiri, A. Silicon Integrated 280 GHz Imaging Chipset With 4 × 4 SiGe Receiver Array and CMOS Source. *IEEE Trans. Terahertz Sci. Technol.* **2015**, *5*, 427–437. [CrossRef]
55. Watanabe, T.; Tombet, S.B.; Tanimoto, Y.; Wang, Y.; Minamide, H.; Ito, H.; Fateev, D.; Popov, V.; Coquillat, D.; Knap, W.; et al. Ultrahigh sensitive plasmonic terahertz detector based on an asymmetric dual-grating gate HEMT structure. *Solid-State Electron. Pergamon* **2012**, *78*, 109–114. [CrossRef]
56. Giliberti, V.; Di Gaspare, A.; Giovine, E.; Boppel, S.; Lisauskas, A.; Roskos, H.G.; Ortolani, M. Heterodyne and subharmonic mixing at 0.6 THz in an AlGaAs/InGaAs/AlGaAs heterostructure field effect transistor. *Appl. Phys. Lett.* **2013**, *103*, 093505. [CrossRef]
57. Sun, J.D.; Sun, Y.F.; Wu, D.M.; Cai, Y.; Qin, H.; Zhang, B.S. High-responsivity, low-noise, room-temperature, self-mixing terahertz detector realized using floating antennas on a GaN-based field-effect transistor. *Appl. Phys. Lett.* **2012**, *100*, 013506. [CrossRef]
58. Rumyantsev, S.; Fobelets, K.; Veksler, D.; Hackbarth, T.; Shur, M. Strained-Si modulation doped field effect transistors as detectors of terahertz and sub-terahertz radiation. *Semicond. Sci. Technol.* **2008**, *23*, 105001. [CrossRef]
59. Spirito, D.; Coquillat, D.; De Bonis, S.L.; Lombardo, A.; Bruna, M.; Ferrari, A.C.; Pellegrini, V.; Tredicucci, A.; Knap, W.; Vitiello, M.S. High performance bilayer-graphene terahertz detectors. *Appl. Phys. Lett.* **2014**, *104*, 061111. [CrossRef]
60. Delgado-Notario, J.; Clericò, V.; Diez, E.; Velázquez-Pérez, J.; Taniguchi, T.; Watanabe, K.; Otsuji, T.; Meziani, Y. Asymmetric dual-grating gates graphene FET for detection of terahertz radiations. *APL Photonics* **2020**, *5*, 066102. [CrossRef]
61. Vicarelli, L.; Vitiello, M.; Coquillat, D.; Lombardo, A.; Ferrari, A.C.; Knap, W.; Polini, M.; Pellegrini, V.; Tredicucci, A. Graphene field-effect transistors as room-temperature terahertz detectors. *Nat. Mater.* **2012**, *11*, 865–871. [CrossRef]
62. Vitiello, M.S.; Coquillat, D.; Viti, L.; Ercolani, D.; Teppe, F.; Pitanti, A.; Beltram, F.; Sorba, L.; Knap, W.; Tredicucci, A. Room-temperature terahertz detectors based on semiconductor nanowire field-effect transistors. *Nano Lett.* **2012**, *12*, 96–101. [CrossRef]
63. Viti, L.; Hu, J.; Coquillat, D.; Politano, A.; Knap, W.; Vitiello, M.S. Efficient terahertz detection in black-phosphorus nano-transistors with selective and controllable plasma-wave, bolometric and thermoelectric response. *Sci. Rep.* **2016**, *6*, 1–10. [CrossRef]
64. Romeo, L.; Coquillat, D.; Pea, M.; Ercolani, D.; Beltram, F.; Sorba, L.; Knap, W.; Tredicucci, A.; Vitiello, M. Nanowire-based field effect transistors for terahertz detection and imaging systems. *Nanotechnology* **2013**, *24*, 214005. [CrossRef]
65. Viti, L.; Hu, J.; Coquillat, D.; Knap, W.; Tredicucci, A.; Politano, A.; Vitiello, M.S. Black phosphorus terahertz photodetectors. *Adv. Mater.* **2015**, *27*, 5567–5572. [CrossRef] [PubMed]
66. Grzyb, J.; Andree, M.; Jain, R.; Heinemann, B.; Pfeiffer, U.R. A Lens-Coupled On-Chip Antenna for Dual-Polarization SiGe HBT THz Direct Detector. *IEEE Antennas Wirel. Propag. Lett.* **2019**, *18*, 2404–2408. [CrossRef]
67. Andree, M.; Grzyb, J.; Jain, R.; Heinemann, B.; Pfeiffer, U.R. A Broadband Antenna-Coupled Terahertz Direct Detector in a 0.13-µm SiGe HBT Technology. In Proceedings of the 14th European Microwave Integrated Circuits Conference (EuMIC), Paris, France, 30 September–1 October 2019; IEEE: Paris, France, 2019; pp. 168–171. [CrossRef]
68. Andree, M.; Grzyb, J.; Jain, R.; Heinemann, B.; Pfeiffer, U.R. A Broadband Dual-Polarized Terahertz Direct Detector in a 0.13-µm SiGe HBT Technology. In Proceedings of the IEEE MTT-S International Microwave Symposium (IMS), Boston, MA, USA, 2–7 June 2019; IEEE: Boston, MA, USA, 2019; pp. 500–503. [CrossRef]

69. De Vroede, A.; Reynaert, P. 23.3 A 605 GHz 0.84 mW Harmonic Injection-Locked Receiver Achieving 2.3 pW/$\sqrt{Hz}$ NEP in 28 nm CMOS. In Proceedings of the IEEE International Solid- State Circuits Conference (ISSCC), San Francisco, CA, USA, 13–22 February 2021; IEEE: San Francisco, CA, USA, 2021; pp. 328–330. [CrossRef]
70. Hillger, P.; Grzyb, J.; Jain, R.; Pfeiffer, U.R. Terahertz Imaging and Sensing Applications With Silicon-Based Technologies. *IEEE Trans. Terahertz Sci. Technol.* **2019**, *9*, 1–19. [CrossRef]
71. Generalov, A.A.; Andersson, M.A.; Yang, X.; Vorobiev, A.; Stake, J. A 400-GHz Graphene FET Detector. *IEEE Trans. Terahertz Sci. Technol.* **2017**, *7*, 614–616. [CrossRef]
72. Bauer, M.; Rämer, A.; Chevtchenko, S.A.; Osipov, K.Y.; Čibiraitė, D.; Pralgauskaitė, S.; Ikamas, K.; Lisauskas, A.; Heinrich, W.; Krozer, V.; et al. A high-sensitivity AlGaN/GaN HEMT terahertz detector with integrated broadband bow-tie antenna. *IEEE Trans. Terahertz Sci. Technol.* **2019**, *9*, 430–444. [CrossRef]
73. Bandurin, D.A.; Svintsov, D.; Gayduchenko, I.; Xu, S.G.; Principi, A.; Moskotin, M.; Tretyakov, I.; Yagodkin, D.; Zhukov, S.; Taniguchi, T.; et al. Resonant terahertz detection using graphene plasmons. *Nat. Commun.* **2018**, *9*. [CrossRef] [PubMed]
74. Bauer, M.; Rämer, A.; Boppel, S.; Chevtchenko, S.; Lisauskas, A.; Heinrich, W.; Krozer, V.; Roskos, H.G. High-sensitivity wideband THz detectors based on GaN HEMTs with integrated bow-tie antennas. In Proceedings of the 2015 10th European Microwave Integrated Circuits Conference (EuMIC), Paris, France, 7–8 September 2015; IEEE: Piscataway, NJ, USA, 2015; pp. 1–4.
75. Sangaré, P.; Ducournau, G.; Grimbert, B.; Brandli, V.; Faucher, M.; Gaquière, C.; De-La-Torre, A.Í.; De-La-Torre, I.Í.; Millithaler, J.F.; Mateos, J.; et al. Experimental demonstration of direct terahertz detection at room-temperature in AlGaN/GaN asymmetric nanochannels. *J. Appl. Phys.* **2013**, *113*, 034305. [CrossRef]
76. Blin, S.; Teppe, F.; Tohme, L.; Hisatake, S.; Arakawa, K.; Nouvel, P.; Coquillat, D.; Pénarier, A.; Torres, J.; Varani, L.; et al. Plasma-wave detectors for terahertz wireless communication. *IEEE Electron Device Lett.* **2012**, *33*, 1354–1356. [CrossRef]
77. Bandurin, D.; Gayduchenko, I.; Cao, Y.; Moskotin, M.; Principi, A.; Grigorieva, I.; Goltsman, G.; Fedorov, G.; Svintsov, D. Dual origin of room temperature sub-terahertz photoresponse in graphene field effect transistors. *Appl. Phys. Lett.* **2018**, *112*, 141101. [CrossRef]
78. Degl'Innocenti, R.; Xiao, L.; Jessop, D.S.; Kindness, S.J.; Ren, Y.; Lin, H.; Zeitler, J.A.; Alexander-Webber, J.A.; Joyce, H.J.; Braeuninger-Weimer, P.; et al. Fast room-temperature detection of terahertz quantum cascade lasers with graphene-loaded bow-tie plasmonic antenna arrays. *ACS Photonics* **2016**, *3*, 1747–1753. [CrossRef]
79. Elkhatib, T.A.; Kachorovskii, V.Y.; Stillman, W.J.; Veksler, D.B.; Salama, K.N.; Zhang, X.C.; Shur, M.S. Enhanced plasma wave detection of terahertz radiation using multiple high electron-mobility transistors connected in series. *IEEE Trans. Microw. Theory Tech.* **2010**, *58*, 331–339. [CrossRef]
80. Wiecha, M.M.; Kapoor, R.; Chernyadiev, A.V.; Ikamas, K.; Lisauskas, A.; Roskos, H.G. Antenna-coupled field-effect transistors as detectors for terahertz near-field microscopy. *Nanoscale Adv.* **2021**. [CrossRef]
81. Schuster, F.; Coquillat, D.; Videlier, H.; Sakowicz, M.; Teppe, F.; Dussopt, L.; Giffard, B.; Skotnicki, T.; Knap, W. Broadband terahertz imaging with highly sensitive silicon CMOS detectors. *Opt. Express* **2011**, *19*, 7827. [CrossRef] [PubMed]
82. Nahar, S.; Gutin, A.; Muraviev, A.; Wilke, I.; Shur, M.; Hella, M.M. Terahertz detection using on chip patch and dipole antenna-coupled GaAs High Electron Mobility Transistors. In Proceedings of the 2014 IEEE MTT-S International Microwave Symposium (IMS2014), Tampa, FL, USA, 1–6 June 2014; IEEE: Piscataway, NJ, USA, 2014; pp. 1–4.
83. Kurita, Y.; Ducournau, G.; Coquillat, D.; Satou, A.; Kobayashi, K.; Boubanga Tombet, S.; Meziani, Y.; Popov, V.; Knap, W.; Suemitsu, T.; et al. Ultrahigh sensitive sub-terahertz detection by InP-based asymmetric dual-grating-gate high-electron-mobility transistors and their broadband characteristics. *Appl. Phys. Lett.* **2014**, *104*, 251114. [CrossRef]
84. Ryu, M.W.; Kim, K.S.; Lee, J.S.; Park, K.; Yang, J.R.; Han, S.T.; Kim, K.R. Performance Enhancement of Plasmonic Sub-Terahertz Detector Based on Antenna Integrated Low-Impedance Silicon MOSFET. *IEEE Electron Device Lett.* **2015**, *36*, 220–222. [CrossRef]
85. Castilla, S.; Terrés, B.; Autore, M.; Viti, L.; Li, J.; Nikitin, A.Y.; Vangelidis, I.; Watanabe, K.; Taniguchi, T.; Lidorikis, E.; et al. Fast and sensitive terahertz detection using an antenna-integrated graphene pn junction. *Nano Lett.* **2019**, *19*, 2765–2773. [CrossRef]
86. Perenzoni, M. Measurement of spatial response of CMOS antenna-coupled FET detector at 325 GHz. In Proceedings of the 2014 39th International Conference on Infrared, Millimeter, and Terahertz waves (IRMMW-THz), Tucson, AZ, USA, 14–19 September 2014; IEEE: Piscataway, NJ, USA, 2014; pp. 1–2.
87. Ali, M.; Perenzoni, M.; Stoppa, D. A methodology to measure input power and effective area for characterization of direct THz detectors. *IEEE Trans. Instrum. Meas.* **2016**, *65*, 1225–1231. [CrossRef]
88. Martín-Mateos, P.; Čibiraitė Lukenskienė, D.; Barreiro, R.; de Dios, C.; Lisauskas, A.; Krozer, V.; Acedo, P. Hyperspectral terahertz imaging with electro-optic dual combs and a FET-based detector. *Sci. Rep.* **2020**, *10*, 1–7. [CrossRef]
89. Hou, H.; Liu, Z.; Teng, J.; Palacios, T.; Chua, S.J. A sub-terahertz broadband detector based on a GaN high-electron-mobility transistor with nanoantennas. *Appl. Phys. Express* **2016**, *10*, 014101. [CrossRef]
90. Regensburger, S.; Preu, S.; Mukherjee, A.K.; Schonhuber, S.; Kainz, M.A.; Winnerl, S.; Klopf, J.M.; Lu, H.; Gossard, A.C.; Unterrainer, K. Broadband Terahertz Detection With Zero-Bias Field-Effect Transistors Between 100 GHz and 11.8 THz With a Noise Equivalent Power of 250 pW/$\sqrt{\text{Hz}}$ at 0.6 THz. *IEEE Trans. Terahertz Sci. Technol.* **2018**, *8*, 465–471. [CrossRef]
91. Qin, H.; Li, X.; Sun, J.; Zhang, Z.; Sun, Y.; Yu, Y.; Li, X.; Luo, M. Detection of incoherent terahertz light using antenna-coupled high-electron-mobility field-effect transistors. *Appl. Phys. Lett.* **2017**, *110*, 171109. [CrossRef]
92. Yang, X.; Vorobiev, A.; Generalov, A.; Andersson, M.A.; Stake, J. A flexible graphene terahertz detector. *Appl. Phys. Lett.* **2017**, *111*, 021102. [CrossRef]

93. Roggenbuck, A.; Schmitz, H.; Deninger, A.; Mayorga, I.C.; Hemberger, J.; Güsten, R.; Grüninger, M. Coherent broadband continuous-wave terahertz spectroscopy on solid-state samples. *New J. Phys.* **2010**, *12*, 043017. [CrossRef]
94. TOPTICA Photonics, Inc. TeraScan 780/1550 Brochure. Available online: https://www.toptica.com/fileadmin/Editors_English/11_brochures_datasheets/01_brochures/toptica_BR_THz_TeraScan.pdf (accessed on 21 February 2021).
95. Deninger, A.J.; Roggenbuck, A.; Schindler, S.; Preu, S. 2.75 THz tuning with a triple-DFB laser system at 1550 nm and InGaAs photomixers. *J. Infrared Millim. Terahertz Waves* **2015**, *36*, 269–277. [CrossRef]
96. Brown, E.R.; Smith, F.W.; McIntosh, K.A. Coherent millimeter-wave generation by heterodyne conversion in low-temperature-grown GaAs photoconductors. *J. Appl. Phys.* **1993**, *73*, 1480–1484. [CrossRef]
97. Stephenson, D.; Strauch, R. Water vapor spectrum near 600 GHz. *J. Mol. Spectrosc.* **1970**, *35*, 494–495. [CrossRef]
98. Andersen, J.; Frandsen, A. Absorption efficiency of receiving antennas. *IEEE Trans. Antennas Propag.* **2005**, *53*, 2843–289. [CrossRef]
99. Socher, E.; Shannan, H.; Kastner, R. On the physical aperture and the power that exits a surface enclosing a receiving antenna. *E-FERMAT* **2015**, *7*, 1–6.
100. Coquillat, D.; Marczewski, J.; Kopyt, P.; Dyakonova, N.; Giffard, B.; Knap, W. Improvement of terahertz field effect transistor detectors by substrate thinning and radiation losses reduction. *Opt. Express* **2016**, 272–281. [CrossRef] [PubMed]
101. Sakhno, M.; Gumenjuk-Sichevska, J.; Sizov, F. Modeling of the substrate influence on multielement THz detector operation. *J. Infrared Millim. Terahertz Waves* **2014**, *35*, 703–719. [CrossRef]
102. Sakhno, M.; Gumenjuk-Sichevska, J.; Sizov, F. Modeling of THz detector antenna on conductive substrate. In Proceedings of the 2016 9th International Kharkiv Symposium on Physics and Engineering of Microwaves, Millimeter and Submillimeter Waves (MSMW), Kharkiv, Ukraine, 20–24 June 2016; pp. 1–3. [CrossRef]
103. Čibiraitė, D.; Bauer, M.; Lisauskas, A.; Krozer, V.; Roskos, H.G.; Rämer, A.; Krozer, V.; Heinrich, W.; Pralgauskaitė, S.; Zdanevičius, J.; et al. Thermal noise-limited sensitivity of FET-based terahertz detectors. In Proceedings of the 2017 International Conference on Noise and Fluctuations (ICNF), Vilnius, Lithuania, 20–23 June 2017; pp. 1–4. [CrossRef]